

# Impact of mergers on LISA parameter estimation for nonspinning black hole binaries

Sean T. McWilliams,<sup>1,\*</sup> James Ira Thorpe,<sup>1</sup> John G. Baker,<sup>1</sup> and Bernard J. Kelly<sup>1,2</sup>

<sup>1</sup>*Gravitational Astrophysics Laboratory, NASA Goddard Space Flight Center, 8800 Greenbelt Rd., Greenbelt, MD 20771, USA*

<sup>2</sup>*CRESST and Department of Physics, University of Maryland,  
Baltimore County, 1000 Hilltop Circle, Baltimore, MD 21250, USA*

(Dated: February 4, 2022)

We investigate the precision with which the parameters describing the characteristics and location of nonspinning black hole binaries can be measured with the Laser Interferometer Space Antenna (LISA). By using complete waveforms including the inspiral, merger and ringdown portions of the signals, we find that LISA will have far greater precision than previous estimates for nonspinning mergers that ignored the merger and ringdown. Our analysis covers nonspinning waveforms with moderate mass ratios,  $q \geq 1/10$ , and total masses  $10^5 \lesssim M/M_\odot \lesssim 10^7$ . We compare the parameter uncertainties using the Fisher matrix formalism, and establish the significance of mass asymmetry and higher-order content to the predicted parameter uncertainties resulting from inclusion of the merger. In real-time observations, the later parts of the signal lead to significant improvements in sky-position precision in the last hours and even the final minutes of observation. For comparable-mass systems with total mass  $M/M_\odot \sim 10^6$ , we find that the increased precision resulting from including the merger is comparable to the increase in signal-to-noise ratio. For the most precise systems under investigation, half can be localized to within  $\mathcal{O}(10 \text{ arcmin})$ , and 10% can be localized to within  $\mathcal{O}(1 \text{ arcmin})$ .

PACS numbers: 04.25.Dm, 04.30.Db, 04.70.Bw, 04.80.Nn 95.30.Sf, 95.55.Ym 97.60.Lf

## I. INTRODUCTION

Gravitational waves carry a tremendous amount of information through the universe. It is the goal of the emerging field of gravitational wave astronomy to access that information and bring it to bear on the problems of astrophysics and cosmology. The current generation of gravitational wave detectors, such as the Laser Interferometer Gravitational-wave Observatory (LIGO) [1], are focused on the detection of gravitational waves from isolated astrophysical systems. LIGO and its contemporaries will also provide some minimal information on the parameters of these systems such as their mass, luminosity distance, and approximate sky position. The quality of this information will be limited by the relatively low signal-to-noise ratios (SNR) expected for LIGO events [2].

The Laser Interferometer Space Antenna (LISA) [3], a space-based detector of gravitational waves in the millihertz band, will detect the inspiral and merger of supermassive black hole binaries (BHBs) with very large SNRs ( $100 \sim 10^4$ ) out to redshifts of  $z \sim 10$  or greater [4, 5]. These large SNRs make it possible to extract a large amount of information from each event including mass, mass ratio, spins, orientation, luminosity distance, and sky position. Because sources of gravitational waves are strongly dominated by gravitational dynamics, and because the waves are expected to propagate through intervening matter with little interaction, these observations may provide an unusually clean and direct measurement

of the source system parameters. Of particular interest are the distance and sky position parameters, which will drive LISA's ability to narrow the set of candidate source galaxies or clusters for merger events, potentially opening up a range of multi-messenger astronomy opportunities. For instance, the coincident measurement of gravitational and electromagnetic signatures from a single source galaxy (i. e. standard sirens [6]) will allow a direct measurement of the redshift-luminosity relationship, thereby constraining the dark-energy equation of state. While cosmological models predict that the dark-energy-dominated era began fairly recently at  $z \sim 1$ , measurements for much larger redshifts are not currently possible by other methods, and the standard siren method is limited only by the achievable range of coincident electromagnetic observation.

Extracting this information requires a waveform model that can provide templates with sufficient fidelity to distinguish between signals with different parameters in the presence of instrumental noise. For BHBs, the complete waveform signal is traditionally divided into three different regimes: the inspiral, which can be described using post-Newtonian (PN) orbital dynamics; the ring-down, which can be treated using black-hole perturbation theory; and the merger, which bridges the two and can be predicted using numerical relativity.

Ideally, an estimate of LISA's ability to measure the parameters of observed BHBs would include the information contained in the complete waveform. However, the difficulty associated with modeling the merger has led the majority of such studies (the exceptions being [7], [8], and [9]) to include only the inspiral portion of the waveform. Until recent advances in numerical relativity [10–12] opened the door to a complete understanding of

---

\*Electronic address: Sean.T.McWilliams@nasa.gov

General Relativity’s predictions for these signals, it was not clear whether theoretical knowledge about the final strongest moments of the signal would be available for system parameter measurements. A naive guess at the consequences of omitting the merger would be that the loss in parameter precision would be proportional to the loss in SNR. This assumes that the two portions of the signal have equal density of information per unit SNR and that that information is independent.

There are two reasons that are sometimes cited for expecting that the effect of the merger on parameter precision will be less than that on SNR. The first is that the merger encompasses very few GW cycles compared with the observed portion of the inspiral and it is expected that information content correlates with the number of cycles. The second is that, in the low-frequency limit, the sensitivity of LISA to parameters such as sky position is entirely generated by the orbital motion of the LISA constellation and the merger is too short in duration to experience a significant orbital modulation.

In this work we investigate the significance of the merger to LISA parameter estimation using quasi-analytic waveforms that are tuned to match the results of numerical relativity. We restrict ourselves to non-spinning binaries with moderate mass ratios ( $q \leq 1/10$ ) and explore the parameter space around a candidate system with total redshifted mass of  $1.33 \times 10^6 M_\odot$ , mass ratio  $q = 1/2$ , and redshift  $z = 1$ . Astrophysically, we expect black holes to have spin. While including spin [13, 14] and mergers each separately improve parameter estimation, it is not known how these effects will combine. Therefore, including both spin effects and mergers will be an important followup to this investigation.

In section II, we discuss the methods employed for generating models of the complete waveform signals and the instrument, and for estimating parameter measurement precision. In section III, we examine LISA’s ability to measure binary black-hole system parameters. The primary novelty of our results is that we assume theoretical knowledge of the complete signal is applied in the observational analysis. We examine the impact of including the merger and higher harmonic content (III A) for comparable mass systems near  $10^6 M_\odot$ , the variation of the results across a range of masses (III B) and mass ratios (III C). In (III E) we study how sky position information accumulates in time, which will impact how LISA ultimately interacts with other astronomical instruments. We summarize our key results in section IV.

## II. METHODOLOGY

Before presenting our findings, we will briefly review the steps taken to estimate the precision with which LISA will measure astrophysical parameters using complete waveforms. Theoretical predictions of the strong-field gravitational dynamics and radiation generation must be encoded in a parameterized waveform signal model. We

then need to apply a model of the instrument, including the response to signals and the sources of noise. Finally, we need to estimate the theoretical limit on the uncertainty of the measured signal parameters that could be achieved from a measurement consisting of our realizations of the signal and noise content.

### A. Waveform model

We assume that Einstein’s theory of gravity correctly describes black hole binary systems. While numerical relativity can now treat the final moments of these events, it would be impractical to conduct simulations covering the parameter space of interest. Furthermore, general signal templates must cover the complete signal including the long-lasting inspiral signal which can not be modeled numerically, but which is well-described by the post-Newtonian (PN) approximation [15]. Instead our complete waveform model is based on a variation of the PN treatment that has been “tuned” to approximate the numerical simulation results at late times. Such a model can be tuned using available numerical data, while providing reasonable, if unverified, model signals for arbitrary parameter sets.

In order to investigate LISA’s capabilities for recovering source parameters, we specifically use a waveform model [16] tuned to match the available numerical simulations for nonspinning black hole binaries. This model, referred to as the IRS-EOB model, uses a conventional effective-one-body (EOB) Hamiltonian formalism for the adiabatic inspiral [17]. For the merger-ringdown, a fit to a physically-motivated functional form is employed for the phasing (see Eq. 9 in [16]), while the amplitude is calculated using a model for the flux that is constrained both to be consistent with the inspiral flux through 3.5 PN order, and also to vanish as it approaches the ring-down frequency (referred to as “Model 2” and given by Eq. 19 in [16]). The physical motivation, that the radiation can be treated as though it were being generated by a shrinking rigid rotator, explains the IRS in IRS-EOB, which stands for “implicit rotating source”.

For a unit mass-system ( $m_1 + m_2 = 1$ ), the source model depends only on the remaining intrinsic source parameters, the mass ratio  $q \equiv m_1/m_2$  (where  $m_2 > m_1$ ), and the spins, which we set to vanish for this initial investigation. Throughout this work, we employ waveforms that correspond to  $\sim 10^6 M$  of observation, or  $\sim 3$  months for our fiducial case with  $M = 1.33 \times 10^6 M_\odot$ . Here, we use units of  $G = c = 1$ , so that  $1 M = 4.92 \times 10^{-6} (M/M_\odot)$  seconds. Therefore, lower-mass systems require longer simulations in  $M$ . We are limited computationally from employing longer waveforms, but we have verified that our results do not change significantly (with the single exception of the uncertainty in total system mass) by doubling the waveform length for the lowest-mass cases investigated. We use a model cadence of  $0.5 M$ . The signal is resampled when we apply

the detector's response function, so that the final signal cadence corresponds to a quarter wavelength at the highest frequency reached by the  $\ell = 4$ ,  $m = \pm 4$  harmonics. This is true even for cases where we restrict the calculation to have only quadrupolar content.

After the source calculation, we derive the incident waveforms referenced to the solar system barycenter (SSB), at which point we can apply the response of the LISA detector. Computation of the incident waveform in SSB frame depends on eight additional parameters: the redshifted total system mass  $M = M_o(1+z)$  (with  $M_o$  the rest mass and  $z$  the redshift), luminosity distance  $D_L$ , coalescence time  $t_c$ , and three angles describing the orientation of the binary, for which we use the inclination  $\iota$  (using the convention that  $\iota = 0$  corresponds to the line of sight being coincident with the orbital axis of the binary), initial orbital phase  $\phi_o$  and the polarization phase  $\psi$ . At the source, the emitted radiation can be decomposed in spin-weighted spherical harmonic components  $h_{\ell m}$  of the dimensionless gravitational wave strain (scaled for unit distance from the source). Here the strain is complex-valued to represent both polarization components,  $h \equiv h_+ + ih_\times$ . Specifying the parameters  $(\iota, \phi_o, \psi, M, D_L)$  allows us to calculate the solar-system incident waveform  $h_B$ :

$$h_B = \frac{GM}{c^2 D_L} \left[ e^{2i\psi} \sum_{\ell m} {}^{-2}Y_{\ell m}(\iota, \phi_o) h_{\ell m} \left( \frac{t_c - t}{M} \right) \right], \quad (1)$$

where  ${}^{-2}Y_{\ell m}$  are the spin-weight  $-2$  spherical harmonics [18]. The two additional parameters, the ecliptic latitude  $\beta$  and longitude  $\lambda$ , describe the sky location of the binary in the SSB frame. The dependence on sky location is applied by the instrument response, which we discuss below. We use the vector  $\Lambda^a \equiv (\ln M, \ln D_L, \beta, \lambda, \iota, \phi_o, \psi, t_c)$  to denote the complete set of variable parameters. Note that the dependence on mass ratio,  $q$ , is not explicitly included in  $\Lambda^a$  but is instead implicitly included in the  $h_{\ell m}$ . This is because  $q$  is not varied when computing parameter uncertainties (see section II C), a procedure consistent with that used in [8]. This is equivalent to the assumption that there is no uncertainty in the measurement of  $q$ . We intend to relax this assumption in future investigations.

## B. Instrument model

The instrument model consists of two components: a prescription for converting  $h_B$  into signals observed by the instrument, and a description of the instrument noise.

The LISA instrument consists of a constellation of three spacecraft located at the vertices of an approximately equilateral triangle with a side length of  $5 \times 10^9$  m. The light travel time along each of the six one-way links is monitored using laser interferometry. These individual link measurements are then combined using a technique known as Time Delay Interferometry (TDI) [19] to yield observables that contain gravitational wave signals and suppress instrumental noise. Of the many families of TDI observables [20], the ones most suitable for data analysis are the orthogonalized or “optimal” variables [21]. For this investigation, we have developed a set of orthogonal variables we refer to as “pseudo- $A$ ,  $E$ ,  $T$ ” (hereafter  $\bar{\mathbf{A}} \equiv \{\bar{A}, \bar{E}, \bar{T}\}$ ), which are analogous to the original  $\mathbf{A} \equiv \{A, E, T\}$  variables in [21] except that they are constructed from the Michelson  $\mathbf{X} \equiv \{X, Y, Z\}$  variables rather than the TDI generators  $\boldsymbol{\alpha} \equiv \{\alpha, \beta, \gamma\}$ . The software package *Synthetic LISA* [22] is used to generate the  $\mathbf{X}$  variables from the incident gravitational waveforms,  $h_B$  and the  $\bar{\mathbf{A}}$  variables are then computed as

$$\begin{aligned} \bar{A} &= \frac{Z - X}{2\sqrt{2}} \\ \bar{E} &= \frac{X + Z - 2Y}{2\sqrt{6}} \\ \bar{T} &= \frac{X + Y + Z}{2\sqrt{3}}. \end{aligned} \quad (2)$$

An overall factor of  $\frac{1}{2}$  has been applied to all three formulas to make  $\bar{A}$  and  $\bar{E}$  agree with  $A$  and  $E$  in the low-frequency limit.

*Synthetic LISA* can also be used to model instrument noise. However, *Synthetic LISA* includes statistical fluctuations in its noise-generation algorithms, whereas we are interested in studying parameter uncertainties that result from differences in the incident waveforms for typical instrumental noise levels. We therefore wish to suppress the impact of statistical fluctuations in a given realization of the noise. One way to do this is to generate an ensemble of noise realizations and average them. Satisfactory results can be achieved with a suitable number of averages at the expense of increased computational effort. For this analysis, we have followed the procedure used in [23] to produce analytic estimates of the mean power spectral densities of the noise in the TDI channels directly from the acceleration and optical path length noises in the individual links. This procedure requires making assumptions such as stationary, equal arm lengths. The expressions for the one-sided spectral densities in the  $\bar{\mathbf{A}}$  observables are

$$\begin{aligned} S_{\bar{A}, \bar{E}} &= 2 \sin^2(\Phi) [2(3 + 2 \cos(\Phi) + \cos(2\Phi)) S_{\text{pm}} + (2 + \cos(\Phi)) S_{\text{op}}], \\ S_{\bar{T}} &= 8 \sin^2(\Phi) \sin^2(\Phi/2) [4 \sin^2(\Phi/2) S_{\text{pm}} + S_{\text{op}}], \end{aligned} \quad (3)$$

where  $\Phi \equiv \omega L/c$  and  $L$  is the arm length, expressed as a light-travel time. These expressions are the analog of Eqs. 67 and 68 in [24] and Eqs. 19 and 20 in [21] for the noise response of the original  $\mathbf{A}$ , and we have verified that we duplicate the results in [21] for  $\mathbf{A}$  using  $\alpha$  (accounting for a typographical error which appears in Eq. 20 of [21] which, if corrected, would make it consistent with [24] and with our results).

The quantities  $S_{\text{pm}}$  and  $S_{\text{op}}$  are the one-sided spectral densities of the proof mass acceleration and optical path-length noises, respectively, expressed as equivalent strain. They are modeled as

$$\begin{aligned} S_{\text{pm}} &= 2.5 \times 10^{-48} \left( \frac{f}{1 \text{ Hz}} \right)^{-2} \sqrt{1 + \left( \frac{f}{0.1 \text{ mHz}} \right)^{-2}}, \\ S_{\text{op}} &= 1.8 \times 10^{-37} \left( \frac{f}{1 \text{ Hz}} \right)^2. \end{aligned} \quad (4)$$

The acceleration noise power spectrum in  $S_{\text{pm}}$  includes an additional  $f^{-1}$  reddening below 0.1 mHz to account for the unmodeled behavior of the instrument below the LISA band.

As a check of the expressions in Eq. 3, we used *Synthetic LISA* to model an ensemble of 1000 realizations of noise in the TDI  $\bar{\mathbf{A}}$  channels. Fig. 1 shows a comparison of the mean power spectra of this ensemble with the expressions in Eq. 3. In general, the agreement between the simulated noise and the analytic expressions is quite good. Deviations between the two curves indicate areas of potential concern when evaluating SNR and parameter sensitivity. For example, the analytic noise expressions in Eq. 3 contain nulls at frequencies corresponding to the inverse round-trip times of the constellation. The simulated data, be it signal or noise, is finite at these frequencies due to spectral estimation effects. This leads to a spurious divergent contribution to the SNR and parameter uncertainties at these frequencies. To guard against this, we applied a noise floor of  $10^{-40}(f/1 \text{ Hz})^2$ , eliminating the nulls in the noise response. In addition the ‘flexing’ of the LISA arms due to orbital variations was disabled in *Synthetic LISA* to maintain consistency with the expressions in Eq. 3, which were derived assuming constant arm lengths.

The other area of disagreement between the simulated and analytic noise in Fig. 1 is at the low-frequency end of the  $\bar{T}$  channel. The analytic expression in Eq. 3 predicts that the noise in the  $\bar{T}$  channel should continue to decrease with decreasing frequency, while the simulated noise levels off. As a result of using *Synthetic LISA* to model the signal response, and Eq. 3 to model the noise, there would be a large spurious contribution to SNR and parameter sensitivity at low frequencies, precisely the band where the  $\bar{T}$  channel is not expected to contribute. As the source of this discrepancy has not yet been identified, we have elected to exclude the  $\bar{T}$  channel

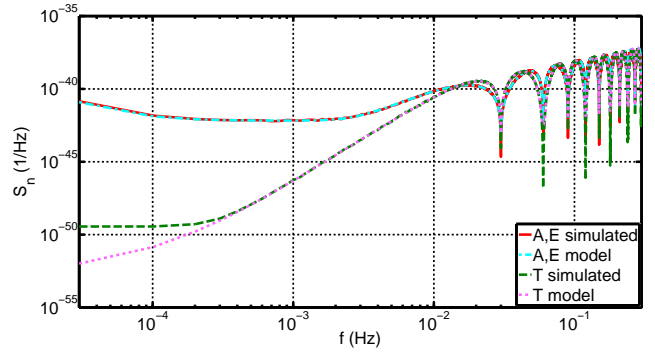


FIG. 1: Comparison of different noise realizations for the  $\bar{A}$ ,  $\bar{E}$ ,  $\bar{T}$  channels. We have employed a noise model (light dash-dotted for  $\bar{A}$  and  $\bar{E}$ , light dotted for  $\bar{T}$ ), and verified that it agrees well with an averaged ensemble of simulated noise using *Synthetic LISA* (dark solid for  $\bar{A}$  and  $\bar{E}$ , dark dashed for  $\bar{T}$ ). Galactic foreground noise is not included in these traces but is included in parameter sensitivity calculations.

in the remainder of our analysis. We note that, since the information from  $\bar{T}$  will be present at high frequencies, its exclusion will lead us to produce conservative uncertainty estimates with systematically worse uncertainties than might be otherwise obtained for higher-mass cases where  $\bar{T}$ -channel response can be non-negligible. Our treatment is consistent with previous studies which have generally neglected the details of LISA high-frequency response. We plan to include  $\bar{T}$  in future work.

The final component of the noise model is the foreground of gravitational waves from unresolved compact binaries. We use the model for the galactic foreground that was developed in [25]. Specifically we add to the expressions for  $S_{\bar{A},\bar{E}}$  in Eq. 3 a galactic foreground noise,  $S_{\text{gal}}$ , given by

$$S_{\text{gal}} = [4\Phi \sin(\Phi)]^2 S_{\text{conf}}, \quad (5)$$

where  $S_{\text{conf}}$  is taken from Eq. 14 of [25]. The contribution from  $S_{\text{gal}}$  is not included in Fig. 1 but is included in all SNR and parameter estimation calculations.

### C. Parameter estimation using the Fisher matrix

To approximate the measurement precision that LISA can achieve, one approach we can take is the Fisher matrix formalism. If the LISA data stream consists of a waveform,  $h(\Lambda^a)$ , embedded in a signal,  $s$ , so that the noise,  $n$ , is given by  $n = s - h$ , then the probability that a signal contains a waveform with the parameter set  $\tilde{\Lambda}^a$  is given by the likelihood function,

$$p(\tilde{\Lambda}^a | s) \propto e^{-\langle h(\tilde{\Lambda}^a) - s | h(\tilde{\Lambda}^a) - s \rangle / 2} \quad (6)$$



where  $\langle \cdots | \cdots \rangle$  is a noise-weighted inner product [26]. The “maximum likelihood” set of parameters,  $\hat{\Lambda}^a$ , is the one that maximizes  $p$ . Errors in the  $\hat{\Lambda}^a$  set of parameters can be assessed by expanding  $p$  around  $\hat{\Lambda}^a$ , such that

$$p(\tilde{\Lambda}^a|s) \propto e^{-\Gamma_{ab}\delta\Lambda^a\delta\Lambda^b/2} \quad (7)$$

where  $\delta\Lambda^a \equiv \tilde{\Lambda}^a - \hat{\Lambda}^a$ . The Fisher information matrix,  $\Gamma_{ab}$ , which is the centerpiece of our subsequent analysis, is defined to be

$$\Gamma_{ab} \equiv \left\langle \frac{\partial h}{\partial \Lambda^a} \left| \frac{\partial h}{\partial \Lambda^b} \right. \right\rangle, \quad (8)$$

where  $a$  and  $b$  are parameter indices. Throughout this work, we calculate the parameter derivatives in Eq. 8 using one-sided differencing, with a fractional step size  $\varepsilon^a = \Delta\Lambda^a$ , where we set  $\Delta = 10^{-4}$  for the coalescence time, and  $\Delta = 10^{-6}$  for all other parameters.

To lowest order in an expansion in  $\text{SNR}^{-1}$ , the covariance matrix,  $\Sigma^{ab}$ , is just the inverse of the Fisher matrix:

$$\Sigma^{ab} = (\Gamma^{ab})^{-1} [1 + \mathcal{O}(\text{SNR}^{-1})], \quad (9)$$

so that  $\sigma^a \equiv \sqrt{\Sigma^{aa}}$  is the standard deviation of parameter  $a$ . The covariance matrix is symmetric, with the off-diagonal terms giving the covariance between parameters, and the diagonal terms giving the variance of each parameter. Because inverting the Fisher matrix to find the covariance matrix is not always valid, we verify our results by testing individual cases at random for each system of interest using Markov Chain Monte Carlo simulations.

Because we use  $\ln M$  and  $\ln D_L$  as parameters, the resulting uncertainties are fractional:

$$\begin{aligned} \sigma^{\ln M} &\approx \sigma^M/M, \\ \sigma^{\ln D_L} &\approx \sigma^{D_L}/D_L. \end{aligned} \quad (10)$$

We therefore express these as fractional uncertainties throughout this work. Though we will refer to the quantities  $\sigma^a$  as “uncertainties” throughout this work, we wish to note that they are a measure of precision, not necessarily accuracy.

Another parameter of interest is the precision of the sky localization, expressed as the area of the uncertainty ellipse on the sky,  $\Omega$ . This is sometimes referred to as  $\Delta\Omega$  or  $\sigma^\Omega$  in the literature, but we simply use  $\Omega$ , given that it is a measure of an area of uncertainty, rather than a measure of uncertainty of an area. To construct this value from our data, we make the approximation

$$\begin{aligned} \Omega &= 2\pi \sqrt{(\sigma^\lambda \sigma^{\cos\beta})^2 - (\Sigma^{\lambda, \cos\beta})^2} \\ &\approx 2\pi \sin\beta \sqrt{(\sigma^\lambda \sigma^\beta)^2 - (\Sigma^{\lambda, \beta})^2}. \end{aligned} \quad (11)$$

We note that generally  $\Omega \neq \pi \sigma^\lambda \sigma^\beta$ , both because we quote median values throughout, and because we define the ellipse as in [27], so that the effect of Eq. 11 is to diagonalize the Fisher sub-matrix formed by  $\beta$  and  $\lambda$ , and thereby calculate the area using the true semi-major and semi-minor axes.

## D. Information Accumulation

One aspect of LISA’s parameter sensitivity that is of interest is the way in which parameter uncertainty evolves with time. A simple way to investigate this is to truncate the signal at a specified sequence of times before merger. To avoid edge effects in the ensuing spectral estimation, the truncated signal is tapered with a raised cosine window with a length of approximately one wave cycle of the quadrupole mode at the time of truncation. The Fisher matrix and covariance matrix are then computed using this truncated signal. By constructing a sequence with progressively later truncation times, one can trace the evolution of parameter uncertainty. Fig. 2 shows the time-evolution of the uncertainty in the ecliptic latitude,  $\beta$ , for an equal-mass system with  $M = 1.33 \times 10^6 M_\odot$  at  $z = 1$ . Three variants of the time curves are shown corresponding to different tapering conventions. The taper either starts at the designated truncation time, ends at that time, or the mid-point of the taper occurs at that time. This distinction, while seemingly trivial, shows the potential impact of slight differences in the treatment of time-domain signals with regard to taper length, type, or placement, as clear differences can be seen in Fig. 2. For early times, the taper prescription does not matter. At later times, the precise taper implementation becomes more important, leading to a time shift between the three curves. In our discussion of information accumulation in section III E, truncation time refers to the mid-point of the taper.

For signals comprising a single harmonic (or rather, a single pair of  $\ell$ ,  $\pm m$  modes, which are complex conjugates of each other for nonspinning waveforms), it is straightforward to repeat this analysis in the frequency domain. This provides an internal consistency check for our code. For each desired truncation time, the instantaneous frequency of the source waveform is used to compute the corresponding signal frequency. The evaluation of the inner product in Eq. 8 is then limited to frequencies below this. The curve in Fig. 2 shows that this approach is consistent with the time-domain approach, at least up to times very near the merger. It would be possible to extend this technique by tracking each mode separately and computing a different frequency cutoff for each. However, we find the time-domain approach to be more straightforward.

## E. Caveats

It is well known that the Fisher-matrix approach is prone to a number of potential pitfalls [28]. In this section, we attempt to address a few of them.

The first potential issue is our approximation of the parameter derivatives,  $\partial h/\partial \Lambda^a$ , using a one-sided finite

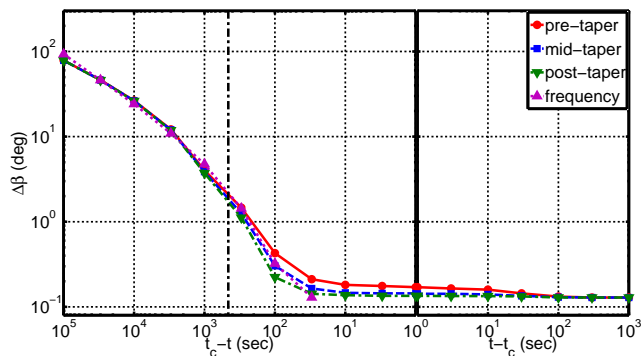


FIG. 2: Estimated improvement in ecliptic latitude uncertainty as a function of signal truncation time,  $t$ , relative to the coalescence time,  $t_c$  for an equal-mass merger with  $M = 1.33 \times 10^6 M_\odot$  at  $z = 1$ . The curves labeled “pre-taper”, “mid-taper”, and “post-taper” were computed using time-domain truncation, with the truncation time corresponding to the end of, middle of, and beginning of a one-radiation-cycle-long taper, respectively. The curve labeled “frequency” was computed using the full waveform but imposing an upper frequency cutoff when evaluating the inner product in Eq. 8 corresponding to the instantaneous signal frequencies at the truncation times. The vertical dash-dotted line corresponds to the Schwarzschild ISCO (see Sec. III A). The vertical thick solid line separates the times prior to merger from the times after merger.

difference approach. As a rough check of the validity of this approximation, we have computed the Fisher and covariance matrices using various finite difference step sizes and verified that the results were consistent. Table I demonstrates that an order of magnitude decrease in the step size changes covariance terms by a few percent at worst.

A related concern is that the Fisher information matrix precision estimates assume that the relevant portion of the likelihood function can be treated as a quadratic function. This assumption should be guaranteed by the large SNR, but is not explicitly verified.

Finally, actual observations will require the implementation of concrete algorithms for exploring the likelihood function, such as those pursued in the Mock LISA Data Challenges [29]. In those Challenges, it has been demonstrated that accuracy may be impacted, for instance, by complicated structure in the likelihood function, including multiple maxima and extended shallow regions. Systematic errors are also possible, for instance, if errors in the theoretical signal predictions should exceed statistical errors [30]. Highly accurate merger waveform predictions, and corresponding models tuned to those predictions, are currently available only for a very limited sampling of specific black hole system configurations. However, this area of study is advancing rapidly, and it now appears that accurate information about the complete

$M$	$D_L$	$\beta$	$\lambda$	$\iota$	$\phi_o$	$\psi$	$t_c$
4.8e-2	5.7e-2	1.3e-2	5.0e-2	4.9e-2	4.8e-2	6.8e-4	4.4e-2
-	3.0e-5	1.9e-4	2.6e-5	1.0e-3	9.1e-4	1.9e-4	4.0e-5
-	-	1.4e-3	1.3e-3	4.0e-4	2.1e-4	3.9e-4	1.5e-4
-	-	-	1.3e-4	5.2e-5	7.1e-3	1.5e-4	5.5e-5
-	-	-	-	5.1e-5	1.1e-2	1.3e-3	1.3e-4
-	-	-	-	-	1.6e-4	2.1e-4	7.1e-3
-	-	-	-	-	-	4.0e-4	5.2e-5
-	-	-	-	-	-	-	3.4e-4

TABLE I: Consistency of the covariance matrix for an equal-mass system with  $M = 1.33 \times 10^6 M_\odot$  at  $z = 1$ . The tabulated quantity is the symmetric matrix  $|1 - \Sigma_{\varepsilon_1}/\Sigma_{\varepsilon_2}|$ , where  $\Sigma_{\varepsilon_i}$  is a covariance matrix calculated using the Fisher matrix method with a one-sided finite-difference step size of  $\varepsilon_i$ . For this comparison,  $\varepsilon_1 = 10^{-6}$  and  $\varepsilon_2 = 10^{-7}$ .

signals throughout the relevant parameter space is likely to be available at the time of LISA’s operation. We therefore focus on the additional source information that may be obtainable when the full signal predictions are applied in the observational analysis.

### III. RESULTS

Since there are variations in the parameter uncertainties across the parameter space, we perform Monte Carlo simulations to find the distribution of uncertainties. For specific choices of masses and luminosity distance (parameters  $M$ ,  $q$ , and  $D_L$ ), we conducted Monte Carlo simulations consisting of 1024 randomly-generated parameter sets for all the cases shown, and have spot-checked that our results do not change significantly if we increase to 8192 parameter sets. The remaining parameters are drawn from uniform distributions, with  $\iota$  drawn from a uniform distribution in  $\cos \iota$  to give uniform sky coverage.

#### A. Adding the merger and higher harmonics

Table II summarizes the improvement in parameter uncertainties resulting from the addition of merger for the cases of equal-mass systems and mass-ratio  $q = 1/2$ , each with a total mass of  $1.33 \times 10^6 M_\odot$  at a redshift  $z = 1$ . We compare the uncertainty estimates obtained with four different options for the waveform models. Two of these options consist of the  $\ell = 2, m = \pm 2$  modes only, with one tapered in time to remove the merger, and the other including the full inspiral-merger-ringdown signal. The midpoint of the taper corresponds to the time when the signal reaches the frequency of the innermost stable circular orbit (ISCO) frequency of a test particle orbit-

$(1+z)M$	$m_1/m_2$	Numerator	Denominator	$\sigma^M/M$	$\sigma^{D_L}/D_L$	$\sigma^\beta$	$\sigma^\lambda$	$\Omega$	$\sigma^\iota$	$\sigma^{\phi_o}$	$\sigma^\psi$	$\sigma^{t_c}$	$\text{SNR}^{-1}$
1.33e6	1/1	$\ell \leq 4$ , ISCO	$\ell \leq 4$ , full	1.2	3.6	4.8	6.4	27	2.3	2.7	5.0	13	3.1
-	-	$\ell =  m  = 2$ , full	$\ell \leq 4$ , full	1.0	2.3	1.8	1.5	2.7	1.8	1.7	2.5	1.2	1.0
-	-	$\ell =  m  = 2$ , ISCO	$\ell \leq 4$ , ISCO	1.0	9.1	6.1	4.0	28	8.3	6.8	7.1	1.2	1.0
1.33e6	1/2	$\ell \leq 4$ , ISCO	$\ell \leq 4$ , full	1.2	3.5	5.5	5.6	29	2.9	2.7	4.8	15	3.2
-	-	$\ell =  m  = 2$ , full	$\ell \leq 4$ , full	1.0	4.5	3.1	2.3	8.2	3.8	3.9	4.8	1.3	1.0
-	-	$\ell =  m  = 2$ , ISCO	$\ell \leq 4$ , ISCO	1.0	16	8.1	6.1	63	16	17	14	1.3	1.0

TABLE II: Ratio of the waveform-model results for median variance of all the extrinsic parameters for two sets of comparable-mass physical systems. The “Numerator” and “Denominator” columns indicate the models compared in constructing the ratios for that row. The models vary by the harmonic content of the waveforms and by whether the merger is included (full) or not (ISCO). For the systems considered here, the fractional loss in estimated precision from ignoring the final merger is comparable to the corresponding loss in SNR and has a greater impact than ignoring higher harmonics. The significance of the higher harmonics is lower when full models are considered, as compared with ISCO-terminated models. The actual median fractional variances for all cases are given in Table III.

ing a Schwarzschild black hole,  $f_{\text{ISCO}} = c^3 / (6^{3/2} \pi G M)$ . Much of the previous systematic work on parameter uncertainties with LISA observations has applied waveform models similar to the ( $\ell = |m| = 2$ , ISCO) option. More recent work has included higher harmonic content[31–35]. Our other two waveform options include modes up to  $\ell \leq 4$ , where one case is again tapered to remove the merger, and the other includes the complete signal.

The top row for each system included in Table II shows the ratio of parameter uncertainties with and without the merger when higher harmonics are included. In each case the inclusion of the merger increases the SNR by roughly a factor of 3. In general terms, if the information contained in the merger waveform is equally rich, as compared with the inspiral waveform, the uncertainties should decrease by a similar factor. This is generally the case for most parameters with the mass uncertainty showing the least improvement and the sky-position, polarization and coalescence-time uncertainties improving most.

The second and third rows for each system in Table II summarize the improvement in uncertainties resulting from the inclusion of higher-harmonic content in the waveforms. The second row shows the improvement in uncertainty when the full waveform is included in each model, while the third row shows the effect of including the higher harmonics with waveform models terminating at ISCO. The latter comparison is roughly similar to previous considerations of the impact of higher harmonics [31–33]. Comparing the second and third rows provides some indication of the independence of information in the higher-harmonics and in the post-ISCO merger. For most parameters the marginal effect of including higher harmonics is not as great when the full-length waveforms are considered as it was for ISCO-terminated waveform models.

In Figs. 3 and 4, we show histograms of our results

for the four waveform model options for the  $q = 1$  and  $q = 1/2$  systems, respectively. The histograms in Fig. 3 agree qualitatively with those presented in our prior work [9]. Quantitatively there is some disagreement, which may be attributed to several factors. Chief among these are the increased duration of the signal ( $\sim 10$  days in the prior work as opposed to  $\sim 3$  months for a comparable mass in this work) and an error in the prior code that omitted a factor of the TDI cadence in the parameter uncertainty estimates.

For both the equal-mass case in Fig. 3, and  $q = 1/2$  in Fig. 4, we see a clear improvement in the level of measurement precision one can expect by including the merger waveform. It appears that, in particular, the parameter  $t_c$  is localized extremely well in both Figs. 3 and 4 for cases that include the merger, relative to the timing precision without the merger. Indeed, for every mass ratio the inclusion of the merger is estimated to result in uncertainties in  $t_c$  that are an order of magnitude or more smaller than the smallest gravitational wave half-period reached by the signal waveforms, which is the shortest time interval over which the signal will contain information content. This dramatic improvement in timing accuracy can be heuristically explained by noting that the merger provides a sharp feature that can be well localized.

The total system mass,  $M$ , is essentially insensitive to the inclusion of the merger or the presence of higher harmonics, and appears to depend entirely on the number of inspiral cycles, as was anticipated in [26]. For this reason, we instead show  $\text{SNR}^{-1}$  in Fig. 4 and in subsequent histograms. This quantity is useful, as it shows the degree of relative improvement in parameter measurement that can be explained by an increase in SNR alone.

The precision of the luminosity distance  $D_L$  and polarization phase  $\psi$  measurements improve by roughly an order-of-magnitude over the quadrupolar inspiral case as

either the merger or higher harmonics are added individually. When both features are added simultaneously, the improvement is “only” a factor of  $\sim 30$ , suggesting that some of the information added by the two features is common.

The inclination  $\iota$  and orbital phase constant  $\phi_o$  show qualitatively different behavior depending on what additional physics is added to the waveform model. For both mass-ratios, we see that the addition of higher harmonics dramatically reduces the long tail of large uncertainties for the parameters in the worst cases of the quadrupole-only results. The addition of the merger, on the other hand, results in an improvement of the most precise determinations of  $\iota$  and  $\phi_o$ , with less effect on the uncertainty of the least accurate parameter sets. Unlike the results for luminosity distance and polarization phase, the overall improvement when both merger and harmonics are included is closer to the product of the individual improvements, indicating that the additional information brought by each is independent.

For the sky angles (the ecliptic latitude  $\beta$  and longitude  $\lambda$ ) the phenomenology of the response to including higher harmonics is roughly reversed from that seen in the inclination and orbital phase angles. In both Figs. 3 and 4, inclusion of higher harmonics most significantly improves the smallest uncertainties in the distribution, with less impact on the largest uncertainties. The addition of the merger, however, appears to be more complicated. For both mass ratios the  $\ell = |m| = 2$  uncertainty distributions for both sky angles appear to uniformly improve. In the  $\ell \leq 4$  distributions, the addition of the merger shows relatively more improvement in the least-accurate side of the distribution. The reduction in uncertainty obtained by adding both features to the waveform model shows less independence than seen with  $\iota$  and  $\phi_o$ . For the  $q = 1/2$  in particular, there is relatively little benefit to adding the higher harmonics once the merger has been included.

### B. Systems with different total masses

With redshifted mass  $1.33 \times 10^6 M_\odot$ , the frequency of the inspiral-merger transition in the signals we have studied so far occurs near the optimal region of LISA’s sensitivity band. Varying the mass shifts this transition frequency (in inverse proportion), thus changing LISA’s relative sensitivity to the inspiral and merger-ringdown signals.

In Fig. 5, we compare three cases, all with a mass ratio  $q = 1/2$  at a redshift  $z = 1$ , and with total masses of  $M = 1.33 \times 10^5 M_\odot$ ,  $1.33 \times 10^6 M_\odot$ , and  $1.33 \times 10^7 M_\odot$ , chosen in part so that the heaviest case can be compared to the results in [8]. In this and subsequent figures, we do not compare results for the measurement of the mass due to the fact that our signal duration is constant in  $M$ , and therefore the lightest systems do not fully span LISA’s band. This was essentially due to computational constraints on the signal length, which we intend to im-

prove upon in future work.

Scaled in units of seconds, we see the best  $t_c$  estimates for the mid-mass case, which merges closest to LISA’s most sensitive band, and therefore has the largest signal-to-noise ratio (SNR). On the other hand, if we were to rescale the curves to measure precision against the time-scale of the source physics,  $M$ , then the largest systems would be seen as most precise.

For the sky position angles the middle mass case outperforms the others by a factor of 2-3, with a broad distribution for the highest mass case. For all other parameters, the lowest mass is easily the worst performer, with the mid-mass system marginally outperforming the largest mass case. In prior investigations that were limited to the inspiral a more precipitous drop in performance occurs for systems with masses approaching  $10^7 M_\odot$ . This is simply a result of the absence of signal, as for such large masses the portion of the total signal that occurs in band for LISA is increasingly dominated by the merger, so that no signal is present when the merger is excluded. This effect is exacerbated in studies that employ a more severe low-frequency cut-off in the LISA sensitivity.

### C. Systems with different mass ratios

We have also examined results for mass ratios other than  $q = 1/2$ . In Fig. 6, we compare three different mass ratios,  $q = 1/2$ ,  $q = 1/4$ , and  $q = 1/10$ , with all three cases again corresponding to a total system mass of  $1.33 \times 10^6 M_\odot$  at a redshift  $z = 1$ .

Varying the mass ratio has surprisingly little effect on the uncertainties. We see that the inverse SNR shows more variation than the parameter uncertainties. This would seem to suggest a balance between the importance of the total signal power and the fraction of that power contained in higher harmonics. To the extent that the relatively small differences among the three cases for most parameters are statistically meaningful, the  $q = 1/10$  case is the worst performer by a small margin for all parameters except  $t_c$ , with an insignificant difference between the  $q = 1/2$  and  $q = 1/4$  cases.

### D. Comparing results

In Table III, we summarize our results by quoting the median parameter uncertainties for all of our data, as well as quoting results for comparable cases from the literature. We note that, as we do not include the mass ratio in our covariance calculation, we are unable to convert to uncertainties in the chirp mass,  $\mathcal{M}_c$ , and reduced mass ratio,  $\mu$ , which are used in [32] and in most of the literature. Furthermore, without explicit knowledge of the covariance between these parameters in the available publications, we are unable to convert the results in the literature into uncertainties in the total mass, so we leave



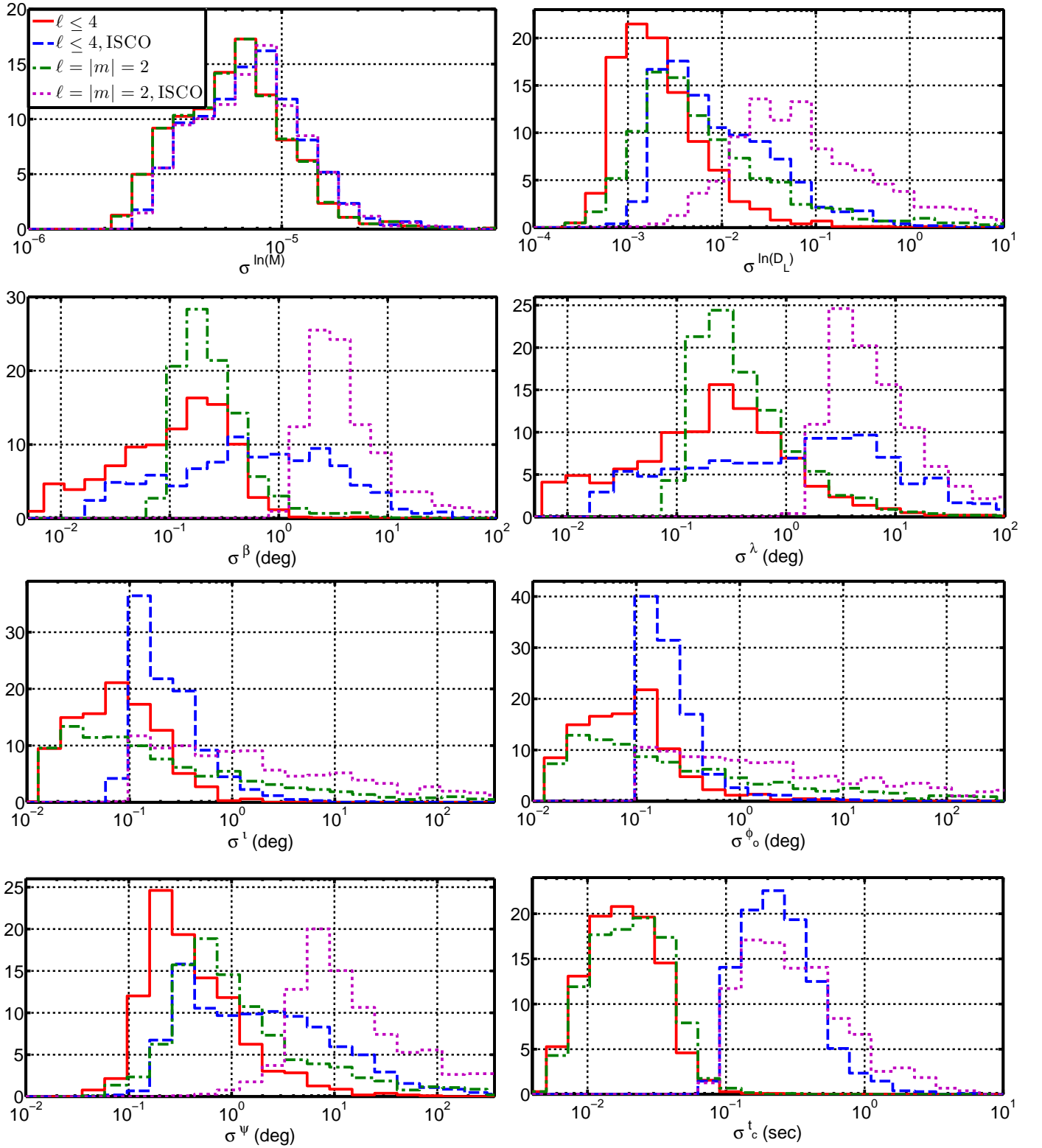


FIG. 3: Uncertainty histograms for  $q = 1$  at redshift  $z = 1$ , corresponding to a total system mass  $M = 1.33 \times 10^6 M_\odot$ , calculated using a full inspiral-merger-ringdown waveform with harmonics  $\ell \leq 4$  (solid), an inspiral waveform truncated at the ISCO as described in Sec. III A (dashed), a full waveform including only quadrupole ( $\ell = 2, m = \pm 2$ ) modes (dash-dotted), and an inspiral waveform including only quadrupole modes (dotted). All histogram bins are normalized by the total number of cases and are expressed as percentages.

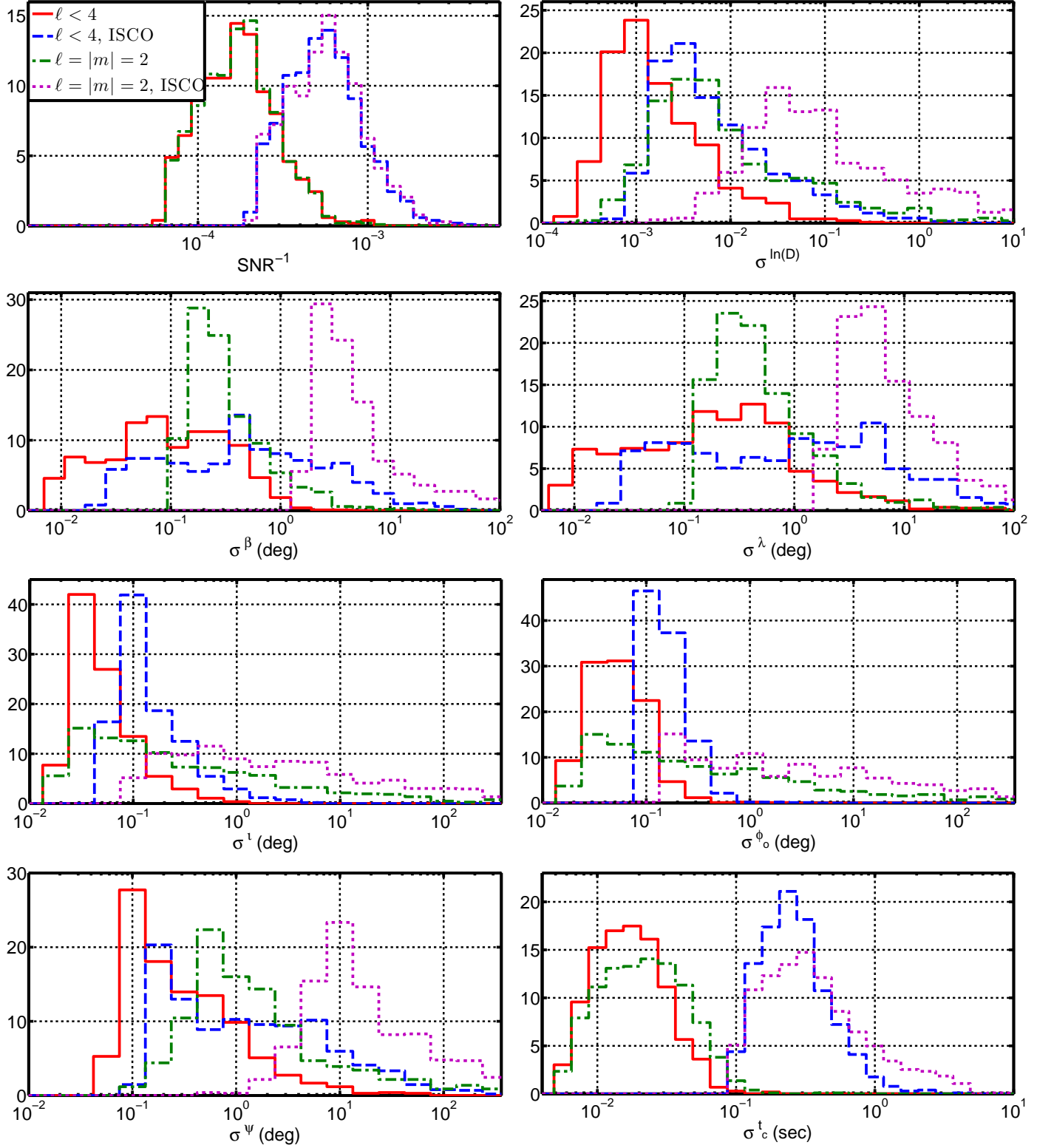


FIG. 4: Uncertainty histograms for  $q = 1/2$  at redshift  $z = 1$ , corresponding to a total system mass  $M = 1.33 \times 10^6 M_\odot$ , calculated using a full inspiral-merger-ringdown waveform with harmonics  $\ell \leq 4$  (solid), an inspiral waveform truncated at the ISCO as described in Sec. III A (dashed), a full waveform including only quadrupole ( $\ell = 2$ ,  $m = \pm 2$ ) modes (dash-dotted), and an inspiral waveform including only quadrupole modes (dotted). All histogram bins are normalized by the total number of cases and are expressed as percentages.

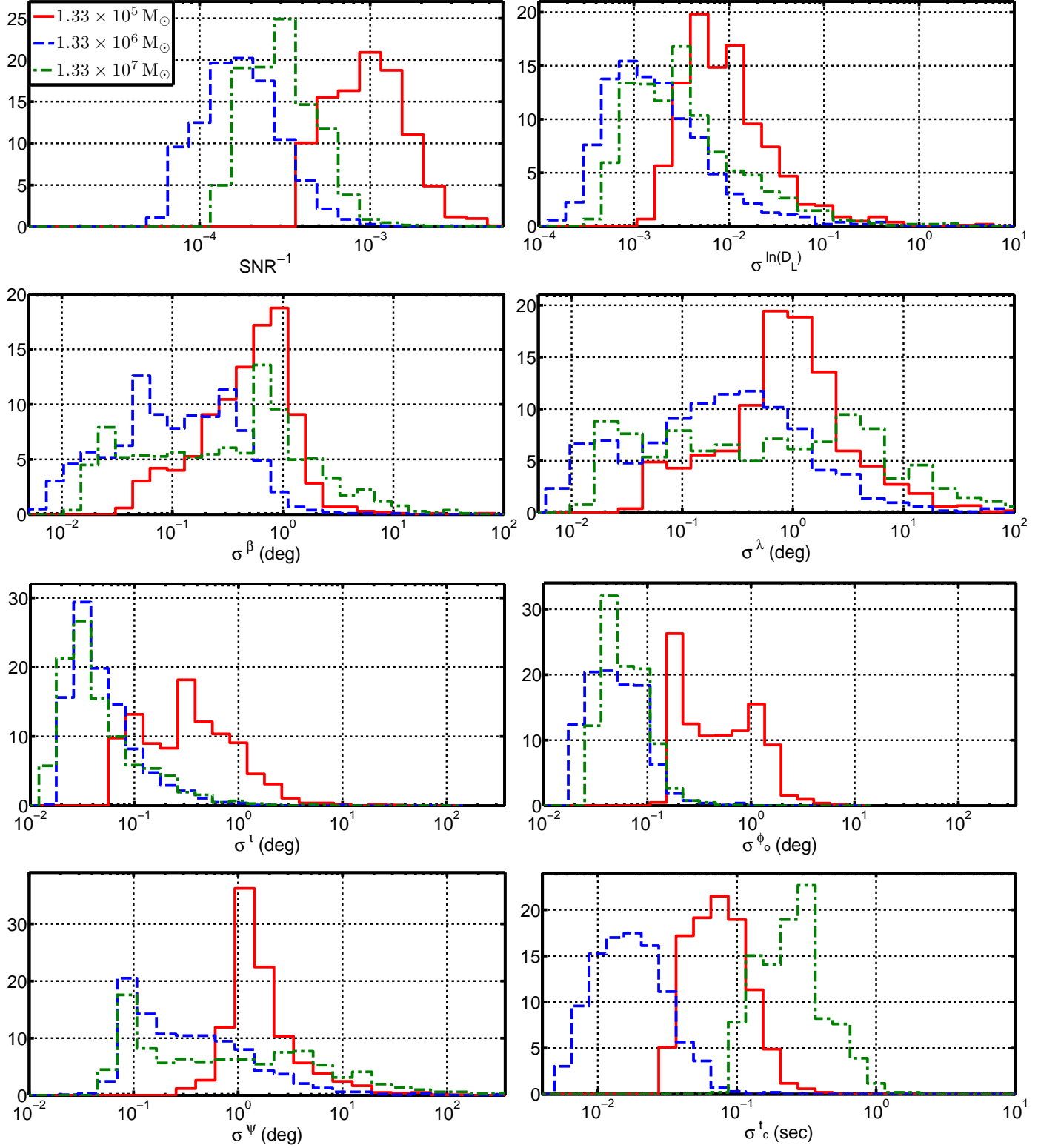


FIG. 5: Uncertainty histograms for  $q = 1/2$  at  $z = 1$ , corresponding to a total system mass  $M = 1.33 \times 10^5 M_\odot$  (solid),  $1.33 \times 10^6 M_\odot$  (dashed), and  $1.33 \times 10^7 M_\odot$  (dash-dotted). All histogram bins are normalized by the total number of cases and are expressed as percentages.

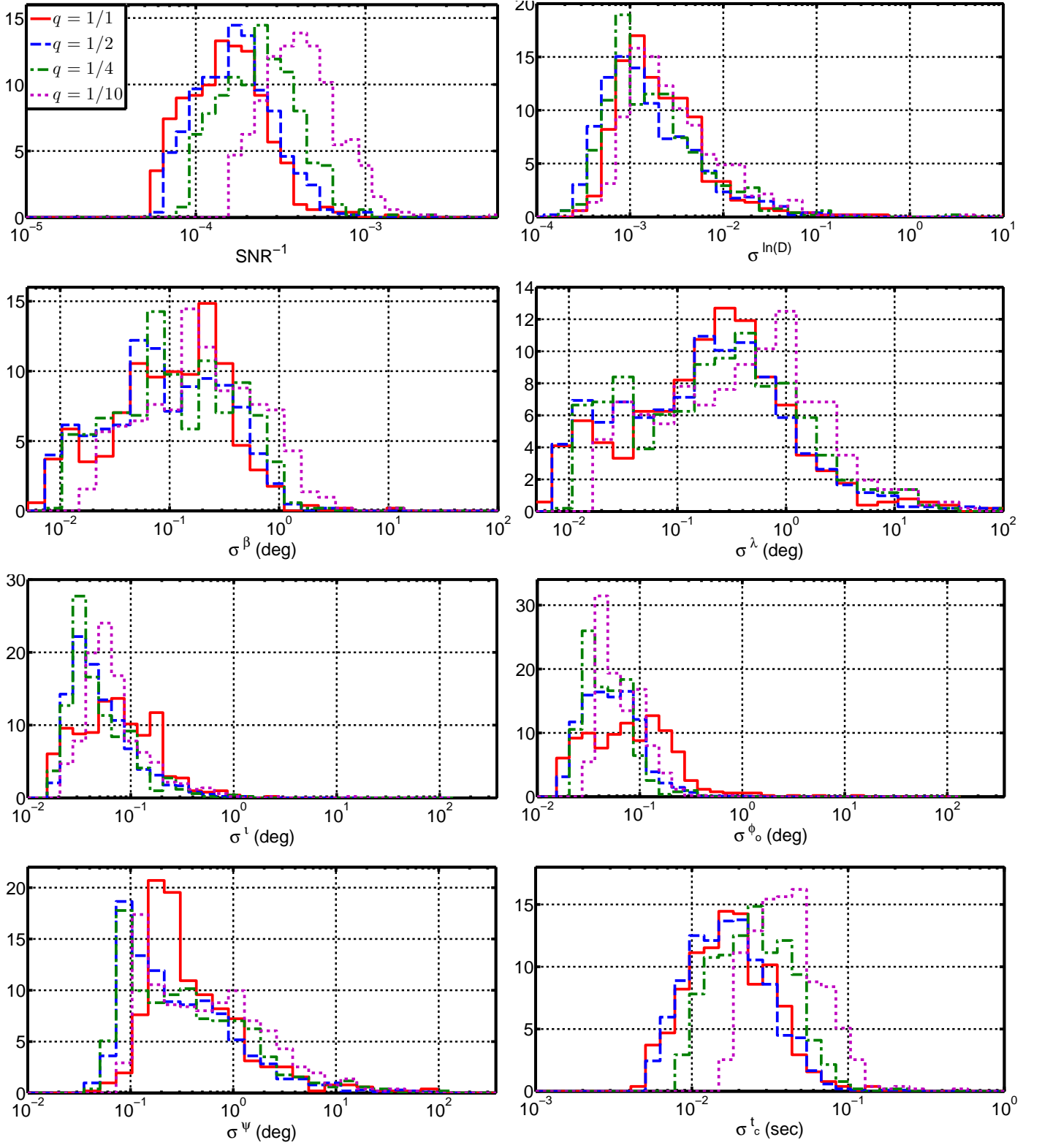


FIG. 6: Uncertainty histograms for  $M = 1.33 \times 10^6 M_{\odot}$  at  $z = 1$ , for mass ratios  $q = 1/1$  (solid),  $1/2$  (dashed), and  $1/4$  (dash-dotted). All histogram bins are normalized by the total number of cases and are expressed as percentages.



the mass out of our comparison in Table III. We do include a comparison of the sky position, calculated using (11).

Of particular note is the discrepancy between our results, and the results found in [8]. Specifically, from their Fig. 1, their median latitude and longitude uncertainties are 0.046 deg and 0.057 deg, respectively, or  $\sim 3$  arcmin as stated in their abstract. However, when running as identical a case as possible with ten cycles prior to merger of a system with  $q = 1/2$  and  $M = 1.33 \times 10^7 M_\odot$ , and using the  $\bar{A}$  and  $\bar{E}$  channels only, we arrive at median estimates of 0.39 deg and 0.63 deg for the latitude and longitude, respectively. This represents an order-of-magnitude disagreement. We note that for a total mass of  $M = 1.33 \times 10^6 M_\odot$ , the median latitude and longitude uncertainties for all mass ratios was within a factor of a few of the localization claimed in [8], with  $q = 1/2$  providing the best localization with median latitude and longitude uncertainties of 0.09 deg (5 arcmin) and 0.18 deg (11 arcmin), respectively, and with 10% of the cases in that ensemble being localized at the  $\sim 1$  arcmin level.

### E. Accumulation of information with time

In actual observations of black hole binaries with LISA, information about the system will be progressively unveiled over time. In particular some estimate of the system parameters may be available in advance of the merger observation. As the system approaches merger the uncertainties of these estimates are expected to decrease sharply [14]. This real-time development is especially important in planning multi-messenger observations. How and when sky position estimates improve as the coalescence proceeds may impact the instruments operational requirements including how frequently data downlinks are required and in planning protected observing periods near the moment of merger. In turn, these operational requirements may influence details of LISA's instrumental design.

In order to compare the evolution in measured parameter precision for different systems, we have calculated the parameter uncertainty for waveforms whose ends are “turned off” via windowing as described earlier. In this section, all the specified times correspond to the time at the mid-point of the applied taper. This procedure is analogous to a realistic procedure for measuring parameters from progressively longer segments of real-time data.

In Fig. 7, we compare the uncertainty in ecliptic latitude  $\beta$  and longitude  $\lambda$  for the equal-mass waveform and the  $q = 1/2$  waveform, both with higher harmonics  $\ell \leq 4$  and restricted to quadrupolar modes ( $\ell = 2, m = \pm 2$ ). The linear-appearing decrease seen in both panels indicates that, over the last several hours before merger, our estimates for uncertainties in the sky position angles are roughly proportional to the time remaining before merger until a couple minutes before “merger” (which we have

defined as the moment at which the  $|\ell| = 2$  mode amplitude peaks). For the cases studied, the dominant ringdown radiation period is about 80 s, roughly setting the scale at which the linear trend levels off. Note that, in some cases the parameter uncertainties may continue to improve after “merger”, drawing on information in the ringdown radiation. The lower pair of curves in each panel are based on the waveform model including the higher harmonics. Consistent with the discussion in Sec. III A, including the harmonics continues to be valuable even late in the observation, after the merger is recorded.

Fig. 8 shows another comparison of latitude uncertainty, for the same systems compared in Fig. 5. Because the parameter being varied is the total system mass, and the mass rescales time, we compare these results using times measured in  $M$  and in seconds. Because these signals are simply mass-rescalings of the same signal in naturalized units, and therefore have identical harmonic content relative to their quadrupolar content, the main factor for differences is the frequency band spanned by the signal, and where that band falls relative to the most sensitive band of the detector. The lowest-mass case,  $M = 1.33 \times 10^5 M_\odot$ , has the largest number of cycles in-band, and therefore performs best at early times. By the time it merges, however, the signal is chirping at frequencies much higher than the most sensitive band for LISA, so the contribution after ISCO is negligible for this case. The mid-mass case,  $M = 1.33 \times 10^6 M_\odot$ , is outperformed by the lowest-mass case at early times. However, because it merges in LISA's most sensitive band, the contribution approaching ISCO and running through the merger and ringdown is far greater than the other cases. Indeed, by the time the full signal has been included, this case yields a more accurate estimate than the lowest-mass case by a factor of  $\sim 2$ . The largest mass,  $M = 1.33 \times 10^7 M_\odot$ , has the fewest cycles in band, so it yields the lowest precision at early times. However, it too has a substantial gain in SNR, relative to the SNR of its inspiral, in the late inspiral through the merger and ringdown, so it too makes gains in precision relative to the lowest-mass case, although unlike the  $M = 1.33 \times 10^6 M_\odot$  case, it does not fully “catch up”, and remains the worst performer of the three.

We compare latitude uncertainty for four different mass ratios in Fig. 9:  $q = 1$ ,  $q = 1/2$ ,  $q = 1/4$ , and  $q = 1/10$ . This comparison again shows a trade-off between the number of in-band cycles and the signal power. Because radiation reaction is weaker for more disparate mass ratios, the  $q = 1/10$  yields the highest precision at early times, despite having significantly less power (the SNR scales as  $\eta$  for the inspiral, and as  $\eta^2$  for the merger [4, 7]). Sky position uncertainty for the smaller- $q$  cases decreases more slowly over most of the last day than the

	$(1+z)M$	$m_1/m_2$	harmonics	merger?	$\sigma^M/M$	$\sigma^{D_L}/D_L$	$\sigma^\beta$	$\sigma^\lambda$	$\Omega$ (deg <sup>2</sup> )	$\sigma^t$	$\sigma^{\phi_o}$	$\sigma^\psi$	$\sigma^{t_c}$	SNR
this work	1.33e5	1/2	$\ell \leq 4$	y	7.0e-6	4.6e-3	0.24	0.39	2.0	0.26	0.34	0.84	4.9e-2	7.4e2
-	1.33e6	1/1	$\ell \leq 4$	y	6.5e-6	1.9e-3	0.12	0.22	0.11	7.8e-2	7.1e-2	0.34	1.8e-2	4.7e3
-	1.33e6	1/2	$\ell \leq 4$	y	7.7e-6	1.3e-3	8.5e-2	0.18	5.6e-2	4.2e-2	5.1e-2	0.23	1.7e-2	4.2e3
-	1.33e6	1/4	$\ell \leq 4$	y	8.8e-6	1.3e-3	0.10	0.24	9.0e-2	4.6e-2	3.9e-2	0.28	4.4e-2	3.8e3
-	1.33e6	1/10	$\ell \leq 4$	y	4.7e-6	2.1e-3	0.19	0.39	0.28	6.0e-2	5.8e-2	0.43	4.4e-2	1.7e3
-	1.33e7	1/2	$\ell \leq 4$	y	1.1e-5	2.9e-3	0.37	0.61	0.64	5.8e-2	3.6e-2	0.70	0.32	2.5e3
-	1.33e6	1/1	$\ell \leq 4$	n	7.6e-6	6.8e-3	0.57	1.4	3.0	0.18	0.19	1.7	0.23	1.5e3
-	1.33e6	1/1	$\ell = 2$	y	6.5e-6	4.4e-3	0.22	0.33	0.30	0.14	0.12	0.86	2.1e-2	4.7e3
-	1.33e6	1/1	$\ell = 2$	n	7.6e-6	6.2e-2	3.5	5.6	83.	1.5	1.3	12.	0.27	1.5e3
-	1.33e6	1/2	$\ell \leq 4$	n	9.3e-6	4.6e-3	0.47	1.0	1.6	0.12	0.14	1.1	0.25	1.3e3
-	1.33e6	1/2	$\ell = 2$	y	7.8e-6	5.9e-3	0.26	0.41	0.46	0.16	0.20	1.1	2.2e-2	4.2e3
-	1.33e6	1/2	$\ell = 2$	n	9.6e-6	7.5e-2	3.8	6.1	100.	1.9	2.4	15.	0.33	1.3e3
-	<sup>a</sup> 1.33e7	1/2	$\ell \leq 4$	y	8.7e-5	2.9e-3	0.39	0.63	0.75	6.9e-2	3.7e-2	0.70	0.73	2.5e3
[8]	1.33e7	1/2	$\ell \leq 4$	y	-	-	4.6e-2	5.7e-2	-	-	-	-	-	-
[32]	4e6	1/1	2.5 PN	n	-	2.5e-2	-	-	4.2	-	-	-	25.	-
-	2.2e6	1/10	2.5 PN	n	-	1.7e-2	-	-	2.6	-	-	-	13.	-
<sup>b</sup> [13]	4e6	1/1	<sup>c</sup> R1.5 PN	n	-	2e-2	-	-	0.6	-	-	-	-	-
<sup>d</sup> [27]	4e6	1/1	R1.5 PN	n	-	7e-2	-	-	0.5	-	-	-	-	-

<sup>a</sup>signal duration is limited to 10 cycles, for comparison to [8]

<sup>b</sup>estimated from histograms in Fig. 2 of [13]

<sup>c</sup>“R” indicates that the amplitude was restricted to the leading order term.

<sup>d</sup>estimated from the results in Table II of [27]

TABLE III: Median fractional variance of all the extrinsic parameters for the cases investigated in this paper, as well as results from the literature for comparable systems. All angles are measured in degrees, and time is measured in seconds. We separate our results into cases where all available information has been included (top portion), and where some information has been suppressed for testing and analysis (bottom portion). For literature results, “X PN” refers to the post-Newtonian order of the model used. All studies set at a fixed source distance of  $z = 1$ , albeit with slightly different cosmological parameters. The results in this work correspond to  $\sim 10^6 M$  of observation, ( $\sim 3$  months for  $M = 1.33 \times 10^6 M_\odot$ ) unless otherwise noted, while the results from the literature correspond to 1 year of observation.

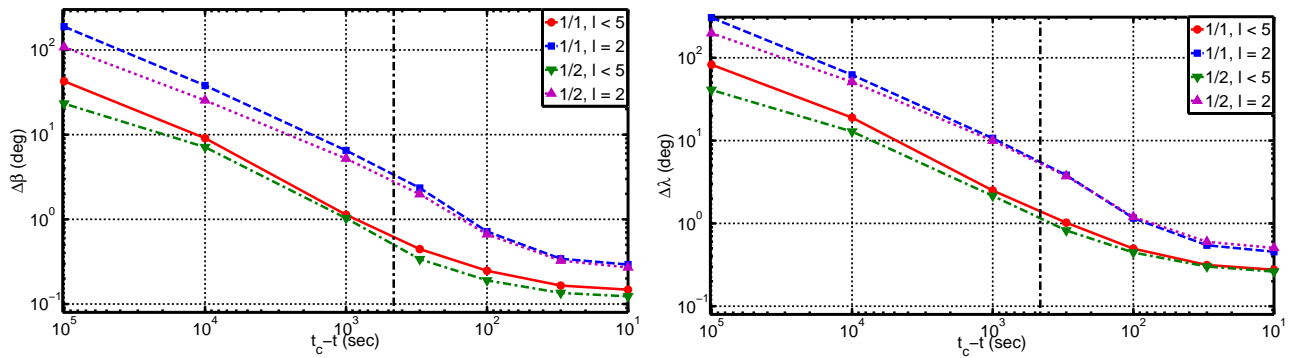


FIG. 7: Comparison of the median ecliptic latitude (left panel) and longitude (right panel) uncertainties as a function of time before the merger for a mass  $M = 1.33 \times 10^6 M_\odot$  at  $z = 1$ , for mass ratios of  $q = 1$  and  $q = 1/2$ . For each mass ratio, we compare the uncertainty for a waveform including harmonics  $\ell \leq 4$  ( $q = 1$ : solid, circles;  $q = 1/2$ : dash-dotted, down arrows), and for waveforms including only the quadrupole ( $\ell = 2, m = \pm 2$ ) modes ( $q = 1$ : dashed, squares;  $q = 1/2$ : dotted, up arrows). The vertical dash-dotted line corresponds to the Schwarzschild ISCO.

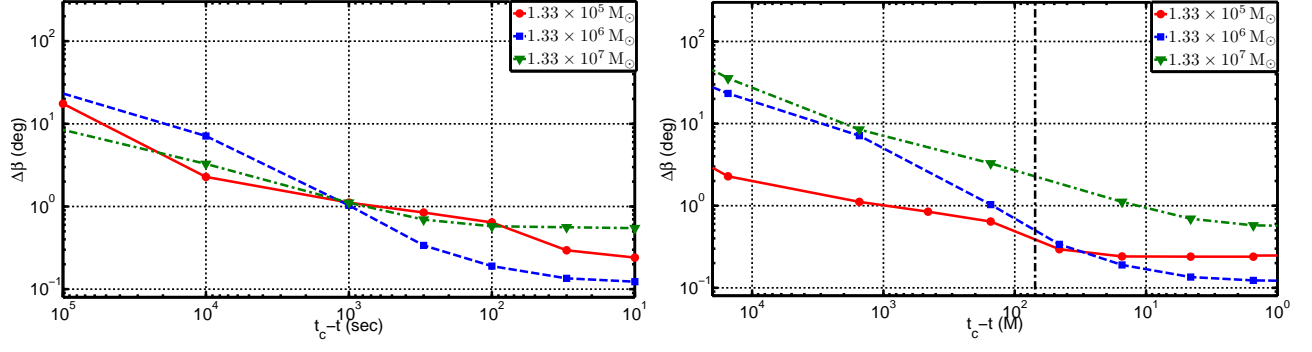


FIG. 8: Comparison of the latitude uncertainty as a function of time before the merger for a mass ratio  $q = 1/2$  at  $z = 1$ , with a total system mass  $M = 1.33 \times 10^5 M_\odot$  (solid, circles),  $M = 1.33 \times 10^6 M_\odot$  (dashed, squares), and  $M = 1.33 \times 10^7 M_\odot$  (dash-dotted, down arrows). In the right panel, the time axis is scaled in units of  $M$ , the physical time-scale of the merger process, rather than seconds. The vertical dash-dotted line corresponds to the Schwarzschild ISCO.

near-linear rate seen for the equal-mass case. By  $\sim 20$  minutes before merger, approaching ISCO, the median uncertainties in  $\beta$  are roughly the same for all mass-ratios shown. At late times, the power content becomes a more dominant factor in further decreasing the uncertainty in  $\beta$ . The equal-mass case contains more signal power in the merger. The  $q = 1/2$  and  $q = 1/4$  cases are nearly optimal, retaining some of the merger signal strength but perhaps benefiting more from stronger harmonic content at late times [16]. Overall final sky-position error estimates are nearly flat for  $1 > q > 1/4$  (see Table III). By  $q = 1/10$  the merger signal power is significantly diminished. While there are still improvements in position estimates after merger, they are notably smaller than those in the other cases.

#### IV. CONCLUSION

We have investigated the precision with which black hole binary system parameters can be measured from LISA observations including merger waveforms in the analysis of nonspinning binaries with moderate mass ratios ( $q \geq 1/10$ ). We have further studied how the expected performance depends on mass ratio and total system mass, and the impact of including or neglecting the merger signal and higher harmonics. The luminosity distance and the polarization phase depend on both the inclusion of the merger and the presence of higher harmonics, although the improvements from including these two elements are not independent. The inclination, the orbital phase constant, the ecliptic latitude and ecliptic longitude also depend on both the merger and the harmonic content. For these parameters the improvements

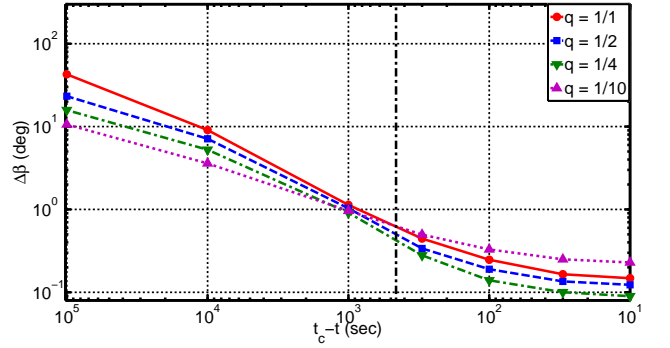


FIG. 9: Comparison of the latitude uncertainty as a function of time before the merger for a mass  $M = 1.33 \times 10^6 M_\odot$  at  $z = 1$ , and mass ratios of  $q = 1$  (solid, circles),  $q = 1/2$  (dashed, squares),  $q = 1/4$  (dotted, down arrows), and  $q = 1/10$  (dash-dotted, up arrows). The vertical dash-dotted line corresponds to the Schwarzschild ISCO frequency.

resulting from including both the merger and higher harmonics are essentially independent.

For comparable-mass systems near  $10^6 M_\odot$ , ignoring the merger reduces the SNR by a factor of  $\sim 3$  and results in a similar loss of median precision in parameter estimation, even more so for the sky position estimates. For sky position, ignoring the merger results in a more significant loss of precision than ignoring higher harmonics. Parameter estimates are roughly independent of mass ratio through  $1 > q > 1/4$ , for sky position in particular, though for smaller mass ratios  $q \lesssim 1/10$  the precision begins to decrease. For  $q = 1/2$ , the best parameter estimates are obtained for systems near  $10^6 M_\odot$ , which merge in the middle of LISA's sensitivity band. Decreasing the

mass by an order of magnitude to  $\sim 10^5 M_\odot$  results in a precision loss of roughly a factor of 5 with a diminished relative contribution from the merger. Increasing the mass to  $\sim 10^7 M_\odot$  results in a similar loss. Though we have left out the effects of spin, including precession, our median sky position precision estimates are similar to those obtained with precession, but ignoring the merger [14]. Each method locates the systems in the sky within  $\mathcal{O}(10 \text{ arcmin})$ . Our best cases ( $\sim$  top 10%) are localized at the level of  $\mathcal{O}(1 \text{ arcmin})$ . We estimate that LISA will usually be able to locate larger mass systems (near  $10^7 M_\odot$ ) quite well, in some cases better than systems with masses near  $10^5 M_\odot$ , and far better than earlier estimates based on inspirals alone. Our results for these more massive systems do not, however, reproduce the preliminary (but widely discussed) extraordinarily precise sky localization results found in [8], though we do achieve such high precision for the  $\sim 10^6 M_\odot$  systems, where both the inspiral and merger are in-band and can

contribute. For equal-mass systems near  $10^6 M_\odot$  the sky angle estimates improve over the last several hours up to a few minutes before merger in rough proportion to the time remaining before merger.

## Acknowledgments

We thank Alessandra Buonanno and Ryan Lang for thorough reviews of the manuscript, and Keith Arnaud and Tuck Stebbins for useful discussions. STM was supported by an appointment to the NASA Postdoctoral Program at the Goddard Space Flight Center, administered by Oak Ridge Associated Universities through a contract with NASA. The simulations were carried out using resources from the NASA Center for Computational Sciences (Goddard Space Flight Center).

- 
- [1] A. A. Abramovici *et al.*, Science **256**, 325 (1992).
  - [2] P. Ajith and S. Bose, Phys. Rev. D **79**, 084032 (2009).
  - [3] K. Danzmann *et al.*, Technical report, Max-Planck-Institut für Quantenoptik, (unpublished), MPQ 233.
  - [4] E. E. Flanagan and S. A. Hughes, Phys. Rev. D **57**, 4535 (1998).
  - [5] J. G. Baker *et al.*, Phys. Rev. D **75**, 124024 (2007).
  - [6] D. E. Holz and S. A. Hughes, Astrophys. J. **629**, 15 (2005).
  - [7] S. T. McWilliams, Ph.D. thesis, The University of Maryland, College Park, Maryland, 2008.
  - [8] S. Babak, M. D. Hannam, S. Husa, and B. F. Schutz (unpublished).
  - [9] J. I. Thorpe *et al.*, Class. Quantum Grav. **26**, 094026 (2009), proceedings of the 7th International LISA Symposium, Barcelona, Spain, 16–20 June 2008.
  - [10] F. Pretorius, Phys. Rev. Lett. **95**, 121101 (2005).
  - [11] J. G. Baker *et al.*, Phys. Rev. Lett. **96**, 111102 (2006).
  - [12] M. Campanelli, C. O. Lousto, P. Marronetti, and Y. Zlochower, Phys. Rev. Lett. **96**, 111101 (2006).
  - [13] A. Vecchio, Phys. Rev. D **70**, 042001 (2004).
  - [14] R. N. Lang and S. A. Hughes, Phys. Rev. D **74**, 122001 (2006), erratum-ibid **75**, 089902 (2007); Erratum-ibid. **77**, 109901 (2008).
  - [15] L. Blanchet, Living Rev. Relativity **9**, 4 (2006), <http://www.livingreviews.org/lrr-2006-4>.
  - [16] J. G. Baker *et al.*, Phys. Rev. D **78**, 044046 (2008).
  - [17] A. Buonanno *et al.*, Phys. Rev. D **76**, 104049 (2007).
  - [18] J. N. Goldberg *et al.*, J. Math. Phys. **8**, 2155 (1967).
  - [19] M. Tinto and J. W. Armstrong, Phys. Rev. D **59**, 102003 (1999).
  - [20] M. Tinto, D. A. Shaddock, J. Sylvestre, and J. W. Armstrong, Phys. Rev. D **67**, 122003 (2003).
  - [21] T. A. Prince, M. Tinto, S. L. Larson, and J. W. Armstrong, Phys. Rev. D **66**, 122002 (2002), arXiv:gr-qc/0209039.
  - [22] M. Vallisneri, Phys. Rev. D **71**, 022001 (2005).
  - [23] F. B. Estabrook, M. Tinto, and J. W. Armstrong, Phys. Rev. D **62**, 042002 (2000).
  - [24] A. Krolak, M. Tinto, and M. Vallisneri, Phys. Rev. D **70**, 022003 (2004).
  - [25] S. E. Timpano, L. J. Rubbo, and N. J. Cornish, Phys. Rev. D **73**, 122001 (2006), arXiv:gr-qc/0504071.
  - [26] C. Cutler and E. E. Flanagan, Phys. Rev. D **49**, 2658 (1994).
  - [27] C. Cutler, Phys. Rev. D **57**, 7089 (1998).
  - [28] M. Vallisneri, Phys. Rev. D **77**, 042001 (2008).
  - [29] Mock LISA Data Challenge home page, <http://astrograves.nasa.gov/docs/mldc/>.
  - [30] C. Cutler and M. Vallisneri, Phys. Rev. D **76**, 104018 (2007).
  - [31] K. G. Arun *et al.*, Phys. Rev. D **76**, 104016 (2007).
  - [32] M. Trias and A. M. Sintes, Class. Quantum Grav. **25**, 184032 (2008).
  - [33] K. G. Arun *et al.*, Class. Quantum Grav. **26**, 094021 (2009).
  - [34] M. Trias and A. M. Sintes, Phys. Rev. D (2008).
  - [35] E. K. Porter and N. J. Cornish, Phys. Rev. D **78**, 064005 (2008).